

# Computational Fluid Dynamics Modeling of Rotating Annular VUV/UV Photoreactor for Water Treatment

## **Authors:**

Minghan Luo, Wenjie Xu, Xiaorong Kang, Keqiang Ding, Taeseop Jeong

*Date Submitted:* 2021-10-14

*Keywords:* water treatment, MB, Computational Fluid Dynamics, photoreactor, VUV

## **Abstract:**

The ultraviolet photochemical degradation process is widely recognized as a low-cost, environmentally friendly, and sustainable technology for water treatment. This study integrated computational fluid dynamics (CFD) and a photoreactive kinetic model to investigate the effects of flow characteristics on the contaminant degradation performance of a rotating annular photoreactor with a vacuum-UV (VUV)/UV process performed in continuous flow mode. The results demonstrated that the introduced fluid remained in intensive rotational movement inside the reactor for a wide range of inflow rates, and the rotational movement was enhanced with increasing influent speed within the studied velocity range. The CFD modeling results were consistent with the experimental abatement of methylene blue (MB), although the model slightly overestimated MB degradation because it did not fully account for the consumption of OH radicals from byproducts generated in the MB decomposition processes. The OH radical generation and contaminant degradation efficiency of the VUV/UV process showed strong correlation with the mixing level in a photoreactor, which confirmed the promising potential of the developed rotating annular VUV reactor in water treatment.

*Record Type:* Published Article

*Submitted To:* LAPSE (Living Archive for Process Systems Engineering)

*Citation (overall record, always the latest version):*

LAPSE:2021.0773

*Citation (this specific file, latest version):*

LAPSE:2021.0773-1

*Citation (this specific file, this version):*

LAPSE:2021.0773-1v1

*DOI of Published Version:* <https://doi.org/10.3390/pr9010079>

*License:* Creative Commons Attribution 4.0 International (CC BY 4.0)

## Article

# Computational Fluid Dynamics Modeling of Rotating Annular VUV/UV Photoreactor for Water Treatment

Minghan Luo <sup>1,2,\*</sup>, Wenjie Xu <sup>1</sup>, Xiaorong Kang <sup>1</sup> , Keqiang Ding <sup>1</sup> and Taeseop Jeong <sup>3</sup>

<sup>1</sup> School of Environmental Engineering, Nanjing Institute of Technology, Nanjing 211167, China; wenjiexu@njit.edu.cn (W.X.); feixiang2004@163.com (X.K.); dingkq@njit.edu.cn (K.D.)

<sup>2</sup> Energy Research Institute, Nanjing Institute of Technology, Nanjing 211167, China

<sup>3</sup> Department of Environmental Engineering, Chonbuk National University, Jeonju 561-756, Korea; jeongts@jbnu.ac.kr

\* Correspondence: leon96201@njit.edu.cn; Tel.: +86-25-86118963

**Abstract:** The ultraviolet photochemical degradation process is widely recognized as a low-cost, environmentally friendly, and sustainable technology for water treatment. This study integrated computational fluid dynamics (CFD) and a photoreactive kinetic model to investigate the effects of flow characteristics on the contaminant degradation performance of a rotating annular photoreactor with a vacuum-UV (VUV)/UV process performed in continuous flow mode. The results demonstrated that the introduced fluid remained in intensive rotational movement inside the reactor for a wide range of inflow rates, and the rotational movement was enhanced with increasing influent speed within the studied velocity range. The CFD modeling results were consistent with the experimental abatement of methylene blue (MB), although the model slightly overestimated MB degradation because it did not fully account for the consumption of OH radicals from byproducts generated in the MB decomposition processes. The OH radical generation and contaminant degradation efficiency of the VUV/UV process showed strong correlation with the mixing level in a photoreactor, which confirmed the promising potential of the developed rotating annular VUV reactor in water treatment.

**Keywords:** VUV; photoreactor; CFD; MB; water treatment



**Citation:** Luo, M.; Xu, W.; Kang, X.; Ding, K.; Jeong, T. Computational Fluid Dynamics Modeling of Rotating Annular VUV/UV Photoreactor for Water Treatment. *Processes* **2021**, *9*, 79. <https://doi.org/10.3390/pr9010079>

Received: 1 December 2020

Accepted: 29 December 2020

Published: 31 December 2020

**Publisher's Note:** MDPI stays neutral with regard to jurisdictional claims in published maps and institutional affiliations.



**Copyright:** © 2020 by the authors. Licensee MDPI, Basel, Switzerland. This article is an open access article distributed under the terms and conditions of the Creative Commons Attribution (CC BY) license (<https://creativecommons.org/licenses/by/4.0/>).

## 1. Introduction

Use of ultraviolet-based photoreactors in water-treatment processes is rapidly increasing, and ultraviolet-based advanced oxidation processes (UV AOPs) have been studied for over 30 years. The H<sub>2</sub>O<sub>2</sub>/UV process presents increased economic cost and technical complexity due to the treatment of residual peroxide, leading to its application only in small and medium-sized water treatment facilities. The VUV/UV process uses ozone-generating mercury lamps that emit 185 nm VUV and 254 nm UV radiation, in which the 185 nm radiation reacts with water to produce hydroxyl radicals ( $\cdot$ OH). Therefore, VUV/UV photodegradation is considered to be a simple and environmentally friendly water-treatment technology with attractive economic potential, which has shown promising potential in wastewater treatment [1]. Although plenty of experiments have yielded promising results at lab-scale, the VUV/UV AOP has not yet been implemented at a full-scale plant in water treatment. There are still problems that impede large-scale application of VUV/UV photoreactors in the water-remediation field. For example, lack of a proper simulation model to predict and analyze the performance of VUV/UV photoreactors is one of the problems hindering their practical implementation. An effective modeling of the VUV/UV process involves the simultaneous solution of momentum equations, mass transfer equations, and radiation energy equations (UV and VUV radiations), along with a complex kinetic scheme of more than 40 reactions.

Computational fluid dynamics (CFD) is an established and effective tool for modeling complex fluid dynamic processes, and has been used extensively for the design, optimization, and scale-up of UV disinfection and oxidation photoreactors in recent years [2,3].

Previous studies have pointed out the importance of using a comprehensive kinetic scheme and a detailed radiation model, including the reflection, refraction, and absorption of photons in UV photoreactors, for CFD simulation. However, few studies about modeling of H<sub>2</sub>O<sub>2</sub>/UV using the CFD method have individually reported the role of 254 nm irradiation in direct photolysis of water, or of the ·OH radical oxidation pathways in the process of removing target pollutants [2,4,5]. Moreover, despite of the similarities between the H<sub>2</sub>O<sub>2</sub>/UV and VUV/UV processes, the associated hydroxyl radical generation mechanisms are different [4–6]. The production of ·OH radicals in VUV/UV systems relies on the photolysis of water at 185 nm irradiation, while hydrogen peroxide photolysis at 254 nm irradiation is the predominant mechanism for the generation of ·OH radicals in H<sub>2</sub>O<sub>2</sub>/UV systems [5]. The direct photolysis of water will generate species such as ·OH, ·H and H<sup>+</sup>, whereas the UV photolysis of hydrogen peroxide produces only ·OH, therefore causing different radical reaction schemes during H<sub>2</sub>O<sub>2</sub>/UV and VUV/UV processes. In addition, the emissions at 185 nm and 254 nm synchronously contribute to the removal of contaminants in a VUV/UV process. In contrast, H<sub>2</sub>O<sub>2</sub>/UV approaches primarily rely on the degradation functions of 254 nm photons. UV light at a wavelength of 185 nm, which plays the key role in ·OH production in VUV/UV AOPs, is transmitted a relatively short distance in solutions. As a result, VUV/UV AOPs normally require better mixing within reactors than UV AOPs, and the effective identification of mixing characteristics of the area around UV lamps is therefore of particular significance for VUV/UV AOP studies.

In this context, this work aimed to develop a comprehensive CFD simulation tool able to make an in-depth analysis of the VUV/UV process applied to water treatment. The proposed computational model integrates a series of sub-models such as hydrodynamic simulations, a multispecies mass transport model, chemical reaction kinetics, and irradiance distribution within the reactor. The radiation field within the reactor was modeled using a nongray discrete ordinate (DO) sub model, which allowed for independent and simultaneous studies of the transportation paths of 185 nm VUV and 254 nm UV. The developed model was experimentally evaluated in a continuous-flow VUV/UV photoreactor for the treatment of a selected pollutant: methylene blue (MB). Finally, we establish and discuss a model for degradation pathways within VUV/UV photoreactors. The results from this study revealed crucial hydrodynamic characteristics in the VUV/UV photoreactor, and provide useful suggestions for the design and optimization of VUV/UV photoreactors, promoting the practical application of VUV/UV techniques in the water-treatment field.

## 2. Materials and Methods

### 2.1. Hydrodynamics

Based on the principles of conservation of mass and momentum, the continuity equations in a rotating annular VUV reactor (RAVR) were described. A three-dimensional computational fluid dynamic model was developed to calculate the local hydrodynamics in the photoreactor.

$$\sum_{i=1}^n \alpha_i = 1 \quad (1)$$

where  $n$  is the total number of phases; the subscript  $i$  represents the gas or liquid phase. The conservation equations are written by performing an ensemble average of the local instantaneous balance for each phase. The motion of each phase is governed by the corresponding mass and momentum conservation equations.

Continuity equation:

$$\frac{\partial(\alpha_i \cdot \rho_i)}{\partial t} + \nabla \cdot (\alpha_i \rho_i \vec{u}_i) = 0 \quad (2)$$

where  $\alpha$ ,  $\rho$ , and  $\vec{u}$  stand for the volume fraction, density, and velocity vector, respectively.

Momentum equation:

$$\frac{\partial(\alpha_i \rho_i \vec{u}_i)}{\partial t} + \nabla \cdot (\alpha_i \rho_i \vec{u}_i \vec{u}_i) = -\alpha_i \nabla P_i + \nabla \cdot \left( \alpha_i \mu_i (\nabla \vec{u}_i - (\nabla \vec{u}_i)^T) \right) + \alpha_i \rho_i \vec{g} \pm \vec{F}_i \quad (3)$$

where  $P$ ,  $\mu$ , and  $\vec{g}$  are the pressure, viscosity, and gravity acceleration, respectively.  $\vec{F}_i$  is the interfacial force acting on phase  $i$  due to the presence of the other phase,  $j$ .

The turbulent dispersion force is the result of the turbulent fluctuations of liquid velocity. In this study, the standard  $k - \varepsilon$  model for single-phase flows was extended for the two-phase flows to simulate the turbulence, which can be described as follows:

$$\frac{\partial}{\partial t} (\alpha_l \rho_l k_l) + \frac{\partial}{\partial x_i} (\alpha_l \rho_l \vec{u}_l k_l) = \frac{\partial}{\partial x_i} \left[ \alpha_l \left( \mu_l + \frac{\mu_{tl}}{\sigma_k} \right) \frac{\partial}{\partial x_i} k_l \right] + \alpha_l \rho_l - \alpha_l \rho_l \varepsilon_l \quad (4)$$

$$\frac{\partial}{\partial t} (\alpha_l \rho_l \varepsilon_l) + \frac{\partial}{\partial x_i} (\alpha_l \rho_l \vec{u}_l \varepsilon_l) = \frac{\partial}{\partial x_i} \left[ \alpha_l \left( \mu_l + \frac{\mu_{tl}}{\sigma_\varepsilon} \right) \frac{\partial}{\partial x_i} \varepsilon_l \right] + \alpha_l \frac{\varepsilon_l}{k_l} (C_{\varepsilon 1} \rho_l - C_{\varepsilon 2} \rho_l \varepsilon_l) \quad (5)$$

where  $C_{\varepsilon 1}$ ,  $C_{\varepsilon 2}$ ,  $\sigma_k$ , and  $\sigma_\varepsilon$  are parameters in the standard  $k - \varepsilon$  model and the following values were selected:  $C_{\varepsilon 1} = 1.44$ ,  $C_{\varepsilon 2} = 1.92$ ,  $\sigma_k = 1.0$ , and  $\sigma_\varepsilon = 1.3$ . In addition, the turbulent viscosities  $\mu_{tl}$  can be computed by other equations [7,8].

## 2.2. Radiative Transfer Model

The radiative transfer equation (RTE) for an absorbing, emitting, and scattering medium at position  $\vec{r}$  in the direction  $\vec{s}$  is as follows:

$$\frac{dI(\vec{r}, \vec{s})}{ds} + (a + \sigma_s) I(\vec{r}, \vec{s}) = an^2 \frac{\sigma T^4}{\pi} + \frac{\sigma_s}{4\pi} \int_0^{4\pi} I(\vec{r}, \vec{s}') \varphi(\vec{s}, \vec{s}') d\Omega' \quad (6)$$

where  $\vec{r}$  and  $\vec{s}$  are position and direction vectors, respectively.  $I$  is the radiation intensity, which depends on position and direction;  $n$  is the refractive index;  $\sigma$  is the Stefan–Boltzmann constant ( $5.67 \times 10^{-8} \text{ Wm}^{-2}\text{K}^{-4}$ );  $a$  is the absorption coefficient;  $\sigma_s$  is the scattering coefficient;  $\varphi$  is the phase function; and  $\Omega'$  is the solid angle. Additionally,  $(a + \sigma_s)s$  is the optical thickness or opacity of the fluid (water mixture). The refractive index  $n$  is important when considering radiation in semitransparent media [7].

## 2.3. Kinetic Reaction Model

In previous studies, detailed kinetic models for VUV systems have been studied to find the perfect batch-scale mixing conditions [4,5]. In this study, 26 types of reaction occurring in the VUV/UV photoreactor (i.e., equilibrium, photochemical, and radical reactions) were summarized, as shown in Table 1, with reference to the previous study. Thus, in the presence of VUV and UV radiation, the main degradation pathways of the species are initiated by the OH radicals produced by the decomposition of water by 185 nm radiation, leading to radical chain reactions induced by 185 and 254 nm radiation.

**Table 1.** Kinetic model of the VUV/UV photoreactor for degradation of MB.

No.	Reaction Equation	Rate Constant	Reference
1	$\text{H}_2\text{O} + h\nu_{185\text{nm}} \rightarrow \text{HO}\cdot + \text{H}\cdot$	$\varnothing_6 = 0.330 \text{ mol/ein}$	Gonzalez et al., 2004 [9]
2	$\text{H}_2\text{O} + h\nu_{185\text{nm}} \rightarrow \text{H}^+ + \text{e}_{\text{aq}}^- + \text{HO}\cdot$	$\varnothing_7 = 0.045 \text{ mol/ein}$	Gonzalez et al., 2004 [9]
3	$\text{H}_2\text{O}_2 + h\nu_{185\text{nm}} \rightarrow 2\text{HO}\cdot$	$\varnothing_8 = 0.500 \text{ mol/ein}$	Gonzalez et al., 2004 [9]
4	$\text{H}_2\text{O}_2 + h\nu_{254\text{nm}} \rightarrow 2\text{HO}\cdot$	$\varnothing_9 = 0.500 \text{ mol/ein}$	Gonzalez et al., 2004 [9]
5	$\text{O}_2 + \text{H}\cdot \rightarrow \text{HO}_2\cdot$	$k_1 = 2.1 \times 10^{10} \text{ M}^{-1}\text{s}^{-1}$	Gonzalez et al., 2004 [9]
6	$\text{O}_2 + \text{e}_{\text{aq}}^- \rightarrow \text{O}_2^{\cdot-}$	$k_2 = 2.0 \times 10^{10} \text{ M}^{-1}\text{s}^{-1}$	Gonzalez et al., 2004 [9]
7	$\text{H}_2\text{O}_2 + \text{OH}\cdot \rightarrow \text{HO}_2\cdot + \text{H}_2\text{O}$	$k_3 = 2.7 \times 10^7 \text{ M}^{-1}\text{s}^{-1}$	Gonzalez et al., 2004 [9]
8	$\text{H}_2\text{O}_2 + \text{HO}_2\cdot \rightarrow \text{OH}\cdot + \text{O}_2 + \text{H}_2\text{O}$	$k_4 = 5.3 \times 10^2 \text{ M}^{-1}\text{s}^{-1}$	Gonzalez et al., 2004 [9]
9	$\text{H}_2\text{O}_2 + \text{O}_2^{\cdot-} \rightarrow \text{OH}\cdot + \text{O}_2 + \text{OH}^-$	$k_5 = 1.6 \times 10^1 \text{ M}^{-1}\text{s}^{-1}$	Gonzalez et al., 2004 [9]
10	$\text{H}_2 + \text{OH}\cdot \rightarrow \text{H}_2\text{O} + \text{H}\cdot$	$k_6 = 6.0 \times 10^7 \text{ M}^{-1}\text{s}^{-1}$	Gonzalez et al., 2004 [9]
11	$\text{OH}\cdot + \text{OH}\cdot \rightarrow \text{H}_2\text{O}_2$	$k_7 = 4.0 \times 10^9 \text{ M}^{-1}\text{s}^{-1}$	Gonzalez et al., 2004 [9]
12	$\text{HO}_2\cdot + \text{HO}_2\cdot \rightarrow \text{H}_2\text{O}_2 + \text{O}_2 + \text{H}_2\text{O}$	$k_8 = 2.6 \times 10^6 \text{ M}^{-1}\text{s}^{-1}$	Gonzalez et al., 2004 [9]
13	$\text{H}\cdot + \text{H}\cdot \rightarrow \text{H}_2$	$k_9 = 1.0 \times 10^{10} \text{ M}^{-1}\text{s}^{-1}$	Gonzalez et al., 2004 [9]
14	$\text{OH}\cdot + \text{H}\cdot \rightarrow \text{H}_2\text{O}$	$k_{10} = 7.0 \times 10^9 \text{ M}^{-1}\text{s}^{-1}$	Gonzalez et al., 2004 [9]
15	$\text{OH}\cdot + \text{O}_2^{\cdot-} \rightarrow \text{O}_2 + \text{HO}^-$	$k_{11} = 7.0 \times 10^9 \text{ M}^{-1}\text{s}^{-1}$	Bielski et al., 1985 [10]
16	$\text{OH}\cdot + \text{HO}_2\cdot \rightarrow \text{H}_2\text{O} + \text{O}_2$	$k_{12} = 6.6 \times 10^9 \text{ M}^{-1}\text{s}^{-1}$	Buxton et al., 1988 [11]
17	$\text{HO}_2\cdot + \text{O}_2^{\cdot-} \rightarrow \text{O}_2 + \text{HO}_2^-$	$k_{13} = 9.7 \times 10^7 \text{ M}^{-1}\text{s}^{-1}$	Buxton et al., 1988 [11]
18	$\text{e}_{\text{aq}}^- + \text{OH}\cdot \rightarrow \text{OH}^-$	$k_{14} = 3.0 \times 10^{10} \text{ M}^{-1}\text{s}^{-1}$	Gonzalez et al., 2004 [9]
19	$2\text{O}_2^{\cdot-} + 2\text{H}_2\text{O} \rightarrow \text{O}_2 + \text{H}_2\text{O}_2 + 2\text{OH}^-$	$k_{15} = 3.0 \times 10^{-1} \text{ M}^{-1}\text{s}^{-1}$	Gonzalez et al., 2004 [9]
20	$\text{e}_{\text{aq}}^- + \text{H}\cdot + \text{H}_2\text{O} \rightarrow \text{H}_2 + \text{OH}^-$	$k_{16} = 2.5 \times 10^{10} \text{ M}^{-1}\text{s}^{-1}$	Gonzalez et al., 2004 [9]
21	$\text{OH}\cdot + \text{HO}_2^- \rightarrow \text{HO}_2\cdot + \text{OH}^-$	$k_{17} = 7.5 \times 10^9 \text{ M}^{-1}\text{s}^{-1}$	Crittenden et al., 1999 [12]
22	$\text{OH}\cdot + \text{OH}^- \rightarrow \text{O}^{\cdot-} + \text{H}_2\text{O}$	$k_{18} = 3.9 \times 10^8 \text{ M}^{-1}\text{s}^{-1}$	Buxton et al., 1988 [11]
23	$\text{H}\cdot + \text{OH}^- \rightarrow \text{e}_{\text{aq}}^- + \text{H}_2\text{O}$	$k_{19} = 3.6 \times 10^8 \text{ M}^{-1}\text{s}^{-1}$	Draganic and Draganic, 1973 [13]
24	$\text{H}_2\text{O}_2 + \text{e}_{\text{aq}}^- \rightarrow \text{OH}\cdot + \text{OH}^-$	$k_{20} = 1.1 \times 10^{10} \text{ M}^{-1}\text{s}^{-1}$	Basfar et al., 2005 [14]
25	$\text{e}_{\text{aq}}^- + \text{H}^+ \rightarrow \text{H}\cdot$	$k_{21} = 2.3 \times 10^{10} \text{ M}^{-1}\text{s}^{-1}$	Basfar et al., 2005 [14]
26	$\text{e}_{\text{aq}}^- + \text{H}_2\text{O} \rightarrow \text{H}\cdot + \text{OH}^-$	$k_{22} = 1.9 \times 10^1 \text{ M}^{-1}\text{s}^{-1}$	Basfar et al., 2005 [14]
27	$\text{H}\cdot + \text{HO}_2\cdot \rightarrow \text{H}_2\text{O}_2$	$k_{23} = 1.1 \times 10^{10} \text{ M}^{-1}\text{s}^{-1}$	Basfar et al., 2005 [14]
28	$\text{H}\cdot + \text{H}_2\text{O}_2 \rightarrow \text{H}_2\text{O} + \text{OH}\cdot$	$k_{24} = 9.0 \times 10^7 \text{ M}^{-1}\text{s}^{-1}$	Basfar et al., 2005 [14]
29	$\text{e}_{\text{aq}}^- + \text{HO}_2^- + \text{H}_2\text{O} \rightarrow 2\text{OH}^- + \text{OH}\cdot$	$k_{25} = 3.5 \times 10^9 \text{ M}^{-1}\text{s}^{-1}$	Mak et al., 1997 [15]
30	$\text{H}\cdot + \text{O}_2^{\cdot-} \rightarrow \text{HO}_2^-$	$k_{26} = 2.0 \times 10^{10} \text{ M}^{-1}\text{s}^{-1}$	Mak et al., 1997 [15]
31	$\text{OH}\cdot + \text{MB} \rightarrow \text{Products}$	$k_{27} = 6.9 \times 10^{10} \text{ M}^{-1}\text{s}^{-1}$	Buxton et al., 1988 [11]

#### 2.4. Geometry of RAVR and System Setup

A simple three-dimensional geometry and a mesh structure developed for the RAVR are shown in Figure 1a. The geometry was created using ANSYS DesignModeler software. The RAVR consisted of a reactor with a total length of 500 mm, a 20 mm diameter lamp and a 20 mm diameter inlet, a 30 mm diameter exit tube, and a 5 mm wall thickness. The inlet exit tube was attached to the reactor in a tangential direction to increase the mixing and reactivity of the reactor. The inlet and outlet entered the reactor tangentially to induce rotational flow in the reactor. The RAVR volume was discretized into 132,529 structured and unstructured volume cells using ANSYS Meshing software.

A flow-through, continuously operating RAVR was used to experimentally evaluate the CFD results. The RAVR system is presented in Figure 1b. The reactor had a tangential inlet and an outlet, with annular and rotation flow configuration, operated with a 17 W low-pressure mercury lamp (G10T5VH, Light Sources Inc., Orange, CT, USA) longitudinally placed at the axial center of the reactor. The inlet flow rate was adjusted to within a 1.963–23.550 L/min range with a defined concentration of MB, and the hydraulic retention time varied from 10 s to 120 s. Flow rates of the MB solutions were controlled by peristaltic pumps.

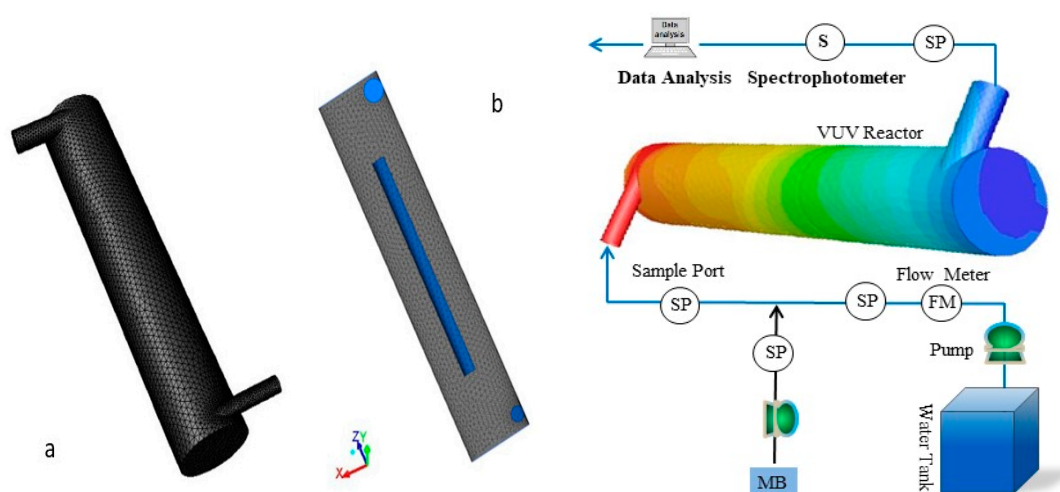


Figure 1. The rotating reactor geometry (a) and the VUV reactor system scheme (b).

### 2.5. Boundary Conditions and Numerical Solution

The inlet velocity had a range of 0.104–1.250 m/s, which corresponded to a flow rate of 1.963 to 23.550 L/min. The inlet concentration of the model contaminant MB was equal to 0.5 ppm. A no-slip boundary condition was imposed on the walls. In addition, zero diffusive flux of species was specified at the walls. As per radiation field boundary conditions, the radiation of lamp was defined as a zero-thickness, semitransparent, nonreflecting wall. The density and viscosity of water considered were  $998.2 \text{ kg/m}^3$  and  $1.003 \times 10^{-3} \text{ Pa}$ , respectively. The refractive indexes of 185 nm and 254 nm were assigned as 1.458 and 1.376, respectively, and the absorption coefficients  $35.67 \text{ (m}^{-1}\text{, UVT = 70\%)}$  and  $12.78 \text{ (m}^{-1}\text{, UVT = 88\%)}$ , respectively.

ANSYS 16.2 Fluent was employed to read the mesh and perform the CFD computations. The segregated steady-state solver was used to solve the governing equations. Second-order upwind discretization schemes were applied except for pressure, for which the standard scheme was selected. The semi-implicit method for pressure linked equations (SIMPLE) algorithm was chosen for the pressure–velocity coupling. The variation of velocity magnitude, model contaminant concentration, and irradiation flux at several points of the computational domain were used as indicators of convergence (at least 20 iterations). Additionally, convergence of the numerical solution was assured by monitoring the scaled residuals to a criterion of at least  $10^{-4}$  for the concentration of MB. While the simulation was always tracked with time, the solution algorithm was run with both steady and transient flow simulations.

### 2.6. Chemicals and Analytical Methods

For the VUV reactor experiments, the chemicals used for experiments were reagent-grade or higher, supplied by Sigma-Aldrich. MB powder was used as purchased without further purification. The MB was diluted separately with ultrapure laboratory water. Distilled water was used in all experiments and analytical determinations. The concentration of MB in the VUV reactor effluent was determined spectrophotometrically following the peak at 664 nm using a UV spectrophotometric probe (UV1800, Shimadzu Co., Marlborough, MA, USA, Kyoto, Japan spectrophotometer). The concentration of hydrogen peroxide was determined via UV spectrophotometry utilizing the  $I_3^-$  method [16].

## 3. Results and Discussion

### 3.1. Hydrodynamics

The fluid velocity magnitudes are shown in Figure 2 for selected cross-sections in the designed RAVR. The results showed that the fluid entered the inlet at a high velocity and

initiated a rotational motion along the wall of the RAVR. For the radial velocity distribution of the reactor, the velocity on the wall of the reactor was higher than that on the surface of central light source of the reactor. Because the rotational flow flowed tangentially onto the reactor wall, part of the kinetic energy was consumed when it reached the light source.

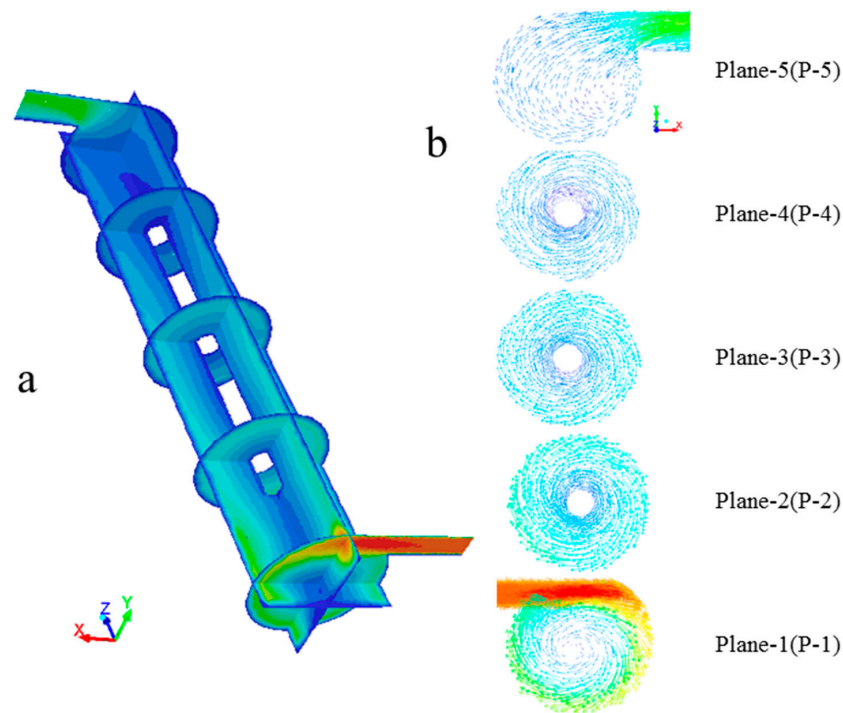


**Figure 2.** Velocity vectors (a) and contours of velocity magnitude (b) along the axial plane at different section planes located at 2 (P-1), 12.5 (P-2), 25 (P-3), 36.5 (P-4), and 48 (P-5) cm positions from the inlet.

As shown by the streamline in Figure 3, the fluid maintained rotational motion from the inlet to the outlet of the reactor, and thus the outflow also presented a rotating flow. Obviously, the rotational flow in the vicinity of outer wall of the reactor showed an upward motion; the rotation force was generated from the flowing force of fluid entering the inlet without additional energy supply. The fluid from the inlet raised along the reactor wall with a high movement velocity. The RAVR integrated the flow characteristics of a continuous-flow stirred-tank reactor (CSTR) and a plug flow reactor (PFR). As mentioned in Section 1, the RAVR is an economical reactor with good mixing function compared with long tubular reactors [17–19] or reactors with internal baffles [3,20,21]. The rotating flow along the VUV lamp in a RAVR reactor plays the role of mixing and extending the fluid-retention time, and there is thus no dead zone in a RAVR reactor.

### 3.2. Pressure Field

Pressure contour analyses of the longitudinal section of the reactor and of Plane-1 to Plane-5 were conducted for the 3.925 L/min inflow rate, and the results are plotted in Figure 4. Pressure increased from the inlet area to outlet area, and decreased along the radial direction from the reactor wall to the central lamp. For Plane-1 (P-1), where the rotation force of the fluid was induced, the entrance position and out-wall area presented high pressure, indicating a whirl flow along the wall surface. The pressure distribution on the cross-section (X–Y plane) of the reactor showed a low-pressure zone in the forced vortex region at the central position due to a high fluid rotating velocity. Since fluid flows from a high-pressure area to a low-pressure area, the longitudinal and radial distribution of pressure in reactor revealed that two circulation flows formed in the reactor: (i) an upward rotating flow along the out-wall surface and (ii) a downward stream adhering to the UV

lamp from the outlet position to the inlet position. Moreover, the pressure distribution shown in Figure 4 is consistent with the streamline shown in Figure 3. When the fluid entered the reactor, it climbed up along the reactor out-wall surface in a rotating flow (outer circulation ring) and flowed into the central part of reactor due to the pressure difference, then went down along the UV lamp at a slow flow rate (inner circulation ring). In this way, the retention time of introduced solutions in the RAVR reactor was extended through two circulation flows, thus enhancing the treatment effect. Additionally, the pressure difference of the RAVR system, which was identified by the ratio of maximum pressure to minimum pressure, was found to change with inflow rates.

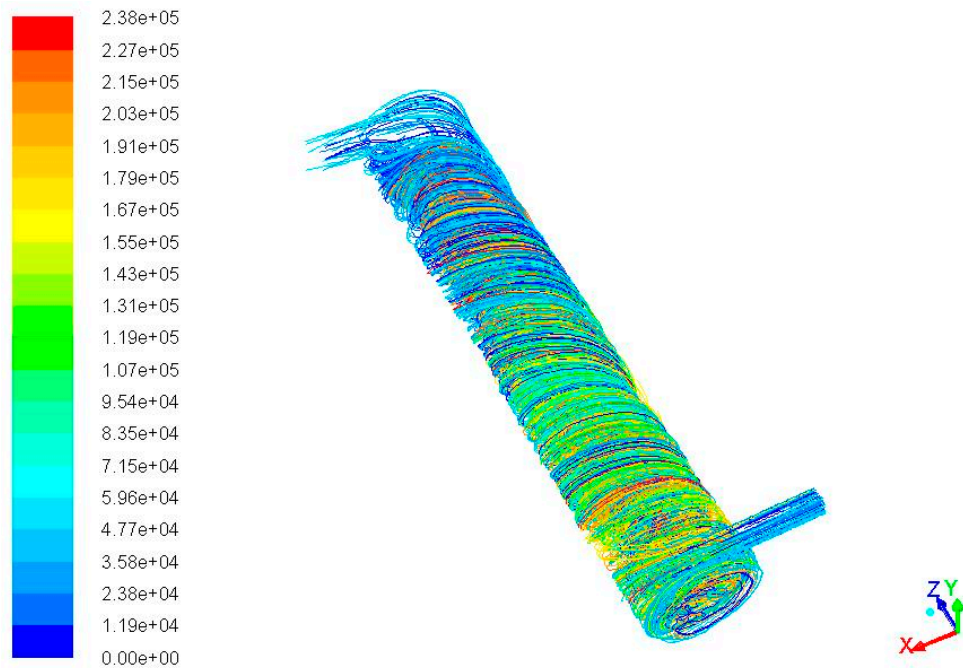


Figure 3. Streamline along the axial plane for inflows at 3.952 L/min velocity.

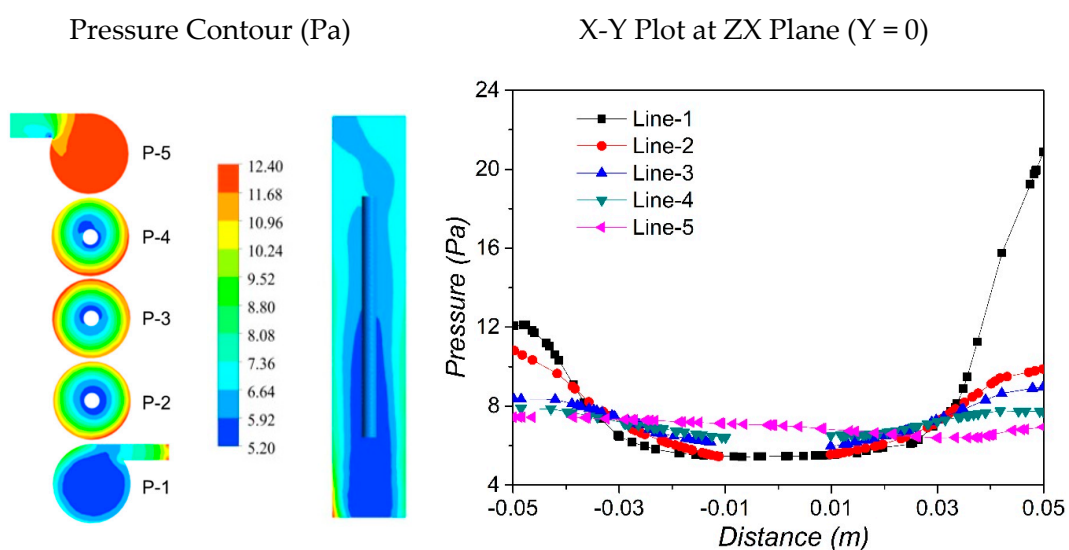
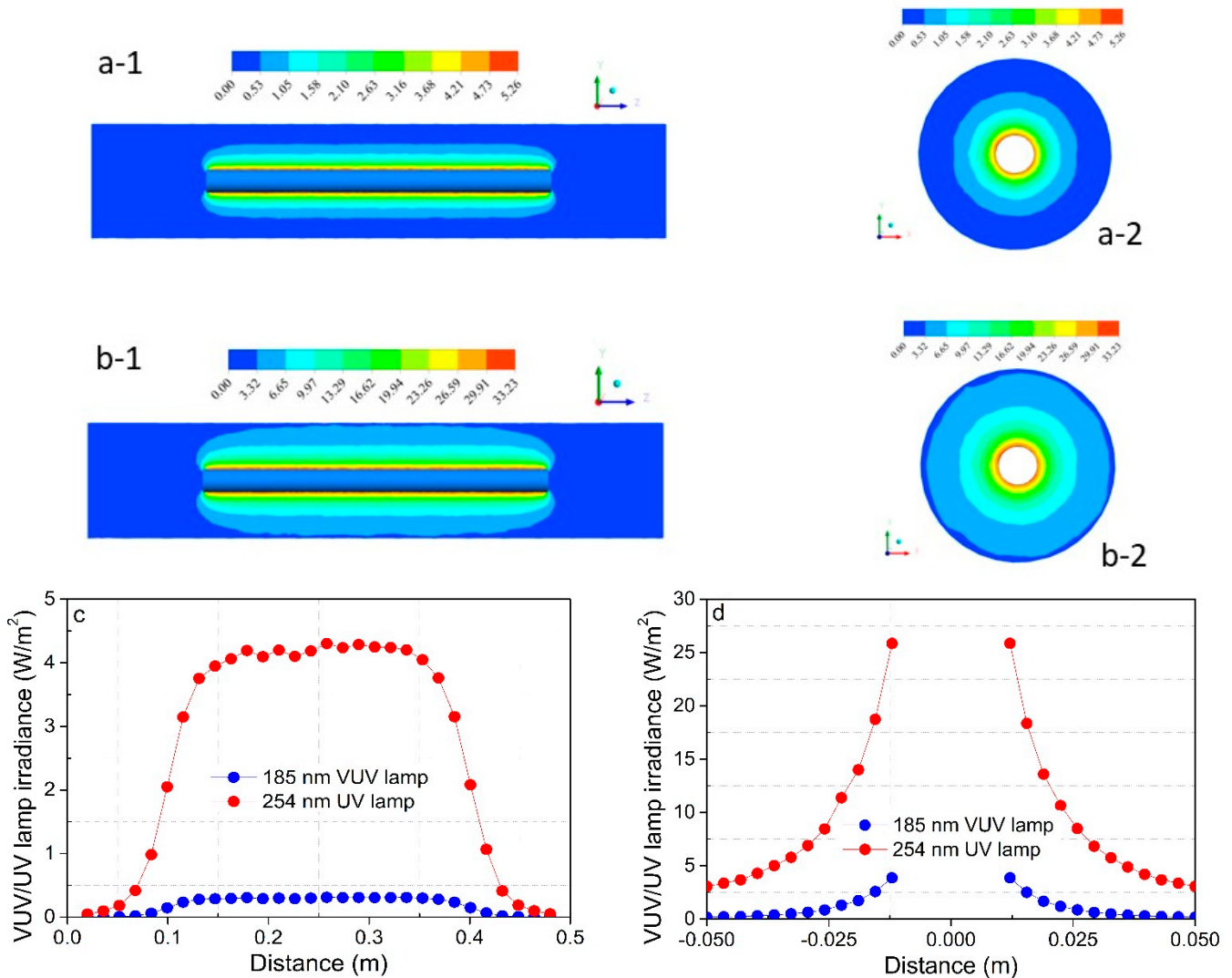


Figure 4. The contour and profiles of pressure in the axial direction of the reactor (including Plane-1 to Plane-5) at 3.925 L/min inflow rate.

### 3.3. UV Radiation

Figure 5 shows the contour distribution of ultraviolet radiation intensity on the X–Z and X–Y cross-sections of the reactor. The ultraviolet radiation at 185 nm, which reacts with and causes the formation of  $\cdot\text{OH}$  radicals, was decreased to almost zero in the wall area around 4 cm away from the lamp due to the limited transmission ability of ultraviolet radiation at 185 nm in water.



**Figure 5.** Local values of ultraviolet irradiance calculated in the whole reaction zone in the X–Z (c) and X–Y (d) planes of the reactor. The longitudinal (a-1, b-1) and radial (a-2, b-2) contours of lamp irradiance. a, 185 nm; b, 254 nm.

### 3.4. Degradation Reaction

The prediction of the RAVR performance was based on CFD modeling simulations, including the specific chemical kinetics of the reactions in the mass balance of involved species. On the basis of the hydrodynamic distribution characteristics of the RAVR, the kinetic responses of the VUV–H<sub>2</sub>O–MB reactions in Table 1 at 3.925 L/min inflow rate are represented in Figure 6, with chemical reaction rates calculated by user defined function (UDF).

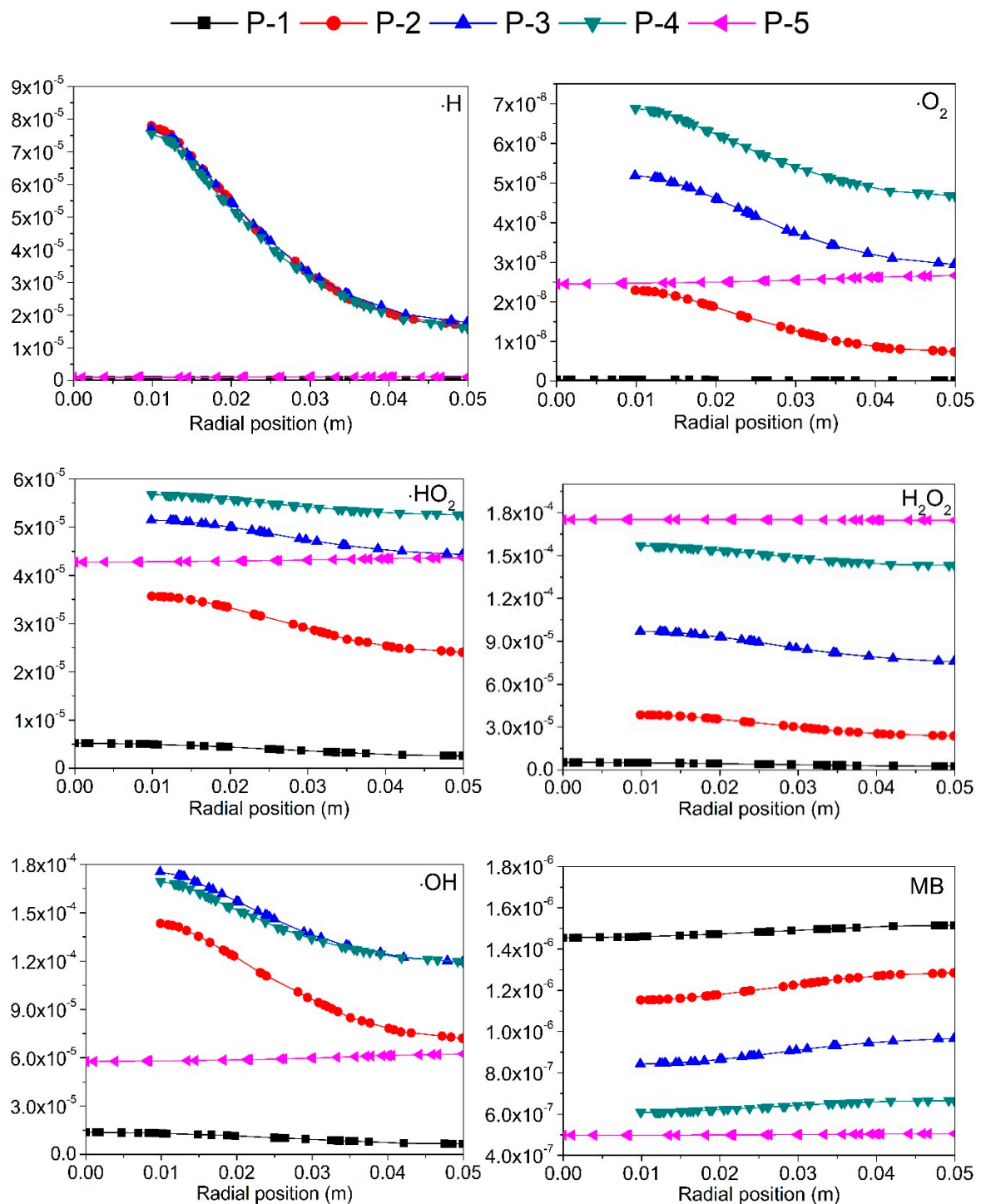


**Figure 6.** Concentration profile (mol/L) of the species in the center line of the plane as a function of the radial position in the reactor (flow rate = 3.925 L/min).

The profiles of molar concentrations of  $\cdot\text{OH}$  radicals (Figure 6) showed a gradual increase from the inlet position to the outlet position (Plane-1 to Plane-4), and then a decrease to a low level on Plane-5. As the Plane-1 was located at the inlet with a small dose of ultraviolet radiation, the concentration of  $\cdot\text{OH}$  radicals were accordingly low. More  $\cdot\text{OH}$  radicals were generated from P-2 to P-4 with increased ultraviolet radiation. Similarly, the amount of radicals was decreased from the center to wall area in the reactor due to the diminished UV radiation. Moreover, comparing the change of  $\cdot\text{OH}$  radicals on different cross-sections, the radical decrease rate from the UV lamp (center position) to the wall

surface was slowed down for Plane-2 to Plane-4. In other words, the concentration gradient of  $\cdot\text{OH}$  radicals on the same cross-section was decreased along the axial direction from inlet to outlet in the RAVR, albeit not as much as in P-1 and P-5. This is mostly because the upward flow accumulated  $\cdot\text{OH}$  radicals and weakened the concentration gradient. It should be noted here that the presented concentration changes of  $\cdot\text{OH}$  radicals in Figure 6 do not reflect the quantitative amounts of  $\cdot\text{OH}$  radicals directly generated from water by UV radiation: in fact, the radiation at 185 nm has a very low ultraviolet transmittance (UVT) and reaches almost zero at a distance of about 3–4 cm from the lamp source. Thus, the concentration profile of hydroxyl radicals reported in Figure 6 is rather a quantitative result based on the advection and diffusion of fluid in the reactor. In addition, the same distribution feature of  $\cdot\text{OH}$  radicals was observed for species like  $\text{H}_2\text{O}_2$ ,  $\cdot\text{H}$ ,  $\cdot\text{HO}_2$ , and  $\cdot\text{O}_2^-$ , except that the concentrations of  $\cdot\text{H}$  on Plane-2 to Plane-4 were very similar. As shown in Table 1, the reaction characteristics of the H radical are quite different from those of other species with higher kinetic parameters. Therefore, a gradient concentration along the radial direction was observed for the H radical at the central position of the reactor (P-2, P-3, and P-4), with higher concentrations near the light source. Furthermore, taking into account that the P-2, P-3, and P-4 profiles fully overlapped, it is possible to state that no appreciable gradient concentration occurred along the longitudinal direction in the central part of the reactor. On the other hand, the MB concentration showed an opposite trend to that of  $\cdot\text{OH}$  radicals as MB was decomposed and removed by the  $\cdot\text{OH}$  radicals. The  $\cdot\text{OH}$ -radical-rich zone coincided with active decomposition reactions of MB. Generally, the low concentration of MB in outflow confirmed the good mixing properties of the designed RAVR, which also implies that developing a process with excellent blending function to enhance the contact between ultraviolet light and each reactant is one important route to increase the efficiency of photolysis reactions.

### 3.5. Comparison of Experimental and Simulation Results

There are two major concerns to be faced in improving the photochemical reactions of VUV/UV AOP. First, the water must be sufficiently irradiated with 185 nm ultraviolet light for the production of  $\cdot\text{OH}$  radicals. In this study, the  $\cdot\text{OH}$  radicals were efficiently generated near the UV lamp (which has a high intensity of ultraviolet radiation at 185 nm) and then quickly diffused across the whole reaction tank. Second, the efficiency of VUV/UV AOP can be significantly enhanced by increasing contact opportunities between the species (like MB) to be treated and the  $\cdot\text{OH}$  radicals generated in the chain reactions. Various methods have been developed based on the two mentioned routes. For example, a pipe-type reactor with a small diameter has been explored for maximization of ultraviolet light intensity [17–19,22]. However, this method has the disadvantage that the long contact time (residence time) required for the reaction can be only obtained by designing a long reaction pipe, which is normally limited by actual situations. Another commonly studied method is the installation of baffles to increase vortices inside the reactor [5,21]. However, this is suitable only for small-scale reactors (like the lab scale) and requires further considerations for application at the industry scale. The adsorption method using an adsorption medium (catalyst) has also been widely studied [21]. Its problem is that the catalysts utilized may hinder the irradiation transmission of ultraviolet light. In conclusion, the design optimization of photoreactors plays a key role in promoting the application of photochemical processes based on  $\cdot\text{OH}$  radical generation in water-treatment or wastewater-treatment fields. The study followed this idea and investigated the possibility of maximizing the utilization of rotational force of the fluid in the designed photoreactor by adjusting the inflow velocity of treated solutions.

The predicted and experimental degradation efficiencies of MB and CFD showed good consistency for the 3.925 L/min inflow rate, as shown in Figure 7. In addition, the pollutant abatement calculated by CFD modeling was slightly lower than the experimental value for all tested inflow velocities.

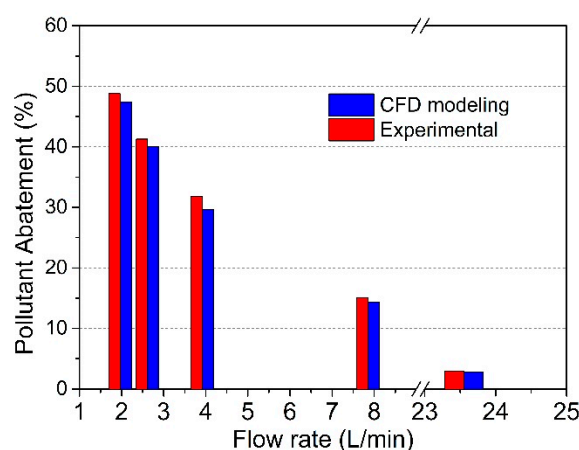


**Figure 7.** Comparison of removal rates of MB of experimental data and CFD-predicted results.

#### 4. Conclusions

This study aimed to develop a novel rotating annular photoreactor with a tangential inlet and outlet to improve the performance of a VUV AOP for increased degradation efficiency of the photoreactor. The flow characteristics as well as the fluid dynamics were investigated and the kinetic model of involved species was simulated to evaluate the reaction characteristics in the designed reactor. Meanwhile, the concentration profiles of  $\cdot\text{OH}$  radicals, target pollutant (MB), and other important reacting species were also determined to assess the reactor properties. The results showed that the introduced fluid was in strong rotational movement inside the reactor across the wide range of influent velocities in this study. Moreover, the rotational movement was enhanced with the increasing of inflow rates in the studied velocity range. The CFD modeling results corresponded well to the experimental degradation of MB. They slightly underestimated degradation due to the limited kinetic analysis about radical annihilation effect from by-products of MB degradation. The results from this study confirmed that the  $\cdot\text{OH}$  radical generation and contaminant degradation efficiency of a VUV/UV process showed strong correlation with the mixing degree in a photoreactor. Therefore, the developed RAVR has high potential to promote the scale-up of VUV/UV AOP systems.

**Author Contributions:** Conceptualization, M.L. and T.J. Data curation, W.X. and X.K. Formal analysis, M.L. Funding acquisition, M.L. Methodology, M.L., W.X., X.K., T.J. and K.D. Validation, M.L. Visualization, M.L. Writing-original draft, M.L. Writing-review & editing, M.L., K.D. and T.J. Project administration, M.L. and T.J. Software, X.K. and W.X. Experiments. All authors have read and agreed to the published version of the manuscript.

**Funding:** This work was funded by Natural Science Research of Jiangsu Higher Education Institutions of China (No.18KJB610006), and Introduction Talent Scientific Research Foundation Project of Nanjing Institute of Technology (No. YKJ201847) and Supported by the Cooperation Fund of Energy Research Institute, Nanjing Institute of Technology (No. CXY201925).

**Conflicts of Interest:** The authors declare no conflict of interest.

#### References

1. Bagheri, M.; Mohseni, M. Computational fluid dynamics (CFD) modeling of VUV/UV photoreactors for water treatment. *Chem. Eng. J.* **2014**, *256*, 51–60. [[CrossRef](#)]
2. Alpert, S.M.; Knappe, D.R.U.; Ducoste, J.J. Modeling the UV/hydrogen peroxide advanced oxidation process using computational fluid dynamics. *Water Res.* **2010**, *44*, 1797–1808. [[CrossRef](#)] [[PubMed](#)]
3. Santoro, D.; Raisee, M.; Moghaddami, M.; Ducoste, J.; Sasges, M.; Liberti, L.; Notarnicola, M. Modeling Hydroxyl Radical Distribution and Trialkyl Phosphates Oxidation in UV–H<sub>2</sub>O<sub>2</sub> Photoreactors Using Computational Fluid Dynamics. *Environ. Sci. Technol.* **2010**, *44*, 6233–6241. [[CrossRef](#)] [[PubMed](#)]
4. Imoberdorf, G.; Mohseni, M. Modeling and experimental evaluation of vacuum-UV photoreactors for water treatment. *Chem. Eng. Sci.* **2011**, *66*, 1159–1167. [[CrossRef](#)]

5. Imoberdorf, G.; Mohseni, M. Kinetic study and modeling of the vacuum-UV photoinduced degradation of 2,4-D. *Chem. Eng. J.* **2012**, *187*, 114–122. [[CrossRef](#)]
6. Li, W.; Li, M.; Wen, D.; Qiang, Z. Development of economical-running strategy for multi-lamp UV disinfection reactor in secondary water supply systems with computational fluid dynamics simulations. *Chem. Eng. J.* **2018**, *343*, 317–323. [[CrossRef](#)]
7. Luo, M.; Chen, Q.; Jeong, T.; Chen, J. Numerical modelling of a three-phase internal air-lift circulating photocatalytic reactor. *Water Sci. Technol.* **2017**, *76*, 3044–3053. [[CrossRef](#)]
8. Wiemann, D.; Mewes, D. Calculation of flow fields in two and three-phase bubble columns considering mass transfer. *Chem. Eng. Sci.* **2005**, *60*, 6085–6093. [[CrossRef](#)]
9. Gonzalez, M.; Oliveros, E.; Worner, M.; Braun, A. Vacuum-ultraviolet photolysis of aqueous reaction systems. *J. Photochem. Photobiol. C* **2004**, *5*, 225–246. [[CrossRef](#)]
10. Bielski, B.H.J.; Cabelli, D.E.; Arudi, R.L.; Ross, A.B. Reactivity of hydroperoxyl/superoxide radicals in aqueous solution. *J. Phys. Chem. Ref. Data* **1985**, *14*, 1041–1100. [[CrossRef](#)]
11. Buxton, G.V.; Greenstock, C.L.; Helman, W.P.; Ross, A.B. Critical Review of rate constants for reactions of hydrated electrons, hydrogen atoms and hydroxyl radicals in Aqueous Solution. *J. Phys. Chem. Ref. Data* **1988**, *17*, 513–886. [[CrossRef](#)]
12. Crittenden, J.C.; Hu, S.; Hand, D.W.; Green, S.A. A kinetic model for H<sub>2</sub>O<sub>2</sub>/UV process in incompletely mixed batch reactor. *Water Res.* **1999**, *33*, 2315–2328. [[CrossRef](#)]
13. Draganic, Z.D.; Draganic, I.G. Studies on the formation of primary yields of hydroxyl radical and hydrated electron in the g-radiolysis of water. *J. Phys. Chem.* **1973**, *77*, 765–772. [[CrossRef](#)]
14. Basfar, A.A.; Khan, H.M.; Al-Shahrani, A.A.; Cooper, W.J. Radiation induced decomposition of methyl tert-butyl ether in water in presence of chloroform: Kinetic modelling. *Water Res.* **2005**, *39*, 2085–2095. [[CrossRef](#)] [[PubMed](#)]
15. Mak, F.T.; Zele, S.R.; Cooper, W.J.; Kurucz, C.N.; Waite, T.D.; Nickelsen, M.G. Kinetic modeling of carbon tetrachloride, chloroform and methylene chloride removal from aqueous solution using the electron beam process. *Water Res.* **1997**, *31*, 219–228. [[CrossRef](#)]
16. Klassen, N.V.; Marchington, D.; McGowan, H.C. H<sub>2</sub>O<sub>2</sub> determination by the I<sub>3</sub>- method and by KMnO<sub>4</sub> titration. *Anal. Chem.* **1994**, *66*, 2921–2925. [[CrossRef](#)]
17. Wols, B.; Harmsen, D.; Wanders-Dijk, J.; Beerendonk, E.; Hofman-Caris, C. Degradation of pharmaceuticals in UV (LP)/H<sub>2</sub>O<sub>2</sub> reactors simulated by means of kinetic modeling and computational fluid dynamics (CFD). *Water Res.* **2015**, *75*, 11–24. [[CrossRef](#)]
18. Li, W.; Li, M.; Bolton, J.R.; Qiang, Z. Configuration optimization of UV reactors for water disinfection with computational fluid dynamics: Feasibility of using particle minimum UV dose as a performance indicator. *Chem. Eng. J.* **2016**, *306*, 1–8. [[CrossRef](#)]
19. Hofman-Caris, R.C.; Harmsen, D.J.; Beerendonk, E.F.; Knol, T.H.; Houtman, C.J.; Metz, D.H.; Wols, B. Prediction of advanced oxidation performance in various pilot UV/H<sub>2</sub>O<sub>2</sub> reactor systems with MP- and LP- and DBD-UV lamps. *Chem. Eng. J.* **2012**, *210*, 520–528. [[CrossRef](#)]
20. Bagheri, M.; Mohseni, M. A study of enhanced performance of VUV/UV process for the degradation of micropollutants from contaminated water. *J. Hazard. Mater.* **2015**, *294*, 1–8. [[CrossRef](#)]
21. Casado, C.; Marugán, J.; Timmers, R.; Muñoz, M.; Vangrieken, R. Comprehensive multiphysics modeling of photocatalytic processes by computational fluid dynamics based on intrinsic kinetic parameters determined in a differential photoreactor. *Chem. Eng. J.* **2017**, *310*, 368–380. [[CrossRef](#)]
22. Yu, H.; Song, L.; Hao, Y.; Lu, N.; Quan, X.; Chen, S.; Zhang, Y.; Feng, Y. Fabrication of pilot-scale photocatalytic disinfection device by installing TiO<sub>2</sub> coated helical support into UV annular reactor for strengthening sterilization. *Chem. Eng. J.* **2016**, *283*, 1506–1513. [[CrossRef](#)]